Journal of Materials Chemistry C

Uniaxial Negative Thermal Expansion Induced by Molecular Rotation in One-Dimensional Supramolecular Assembly with Associated Peculiar Magnetic Behavior

Journal:	*Journal of Materials Chemistry C*
Manuscript ID	TC-ART-11-2022-004874
Article Type:	Paper
Date Submitted by the Author:	16-Nov-2022
Complete List of Authors:	Takahashi, Kiyonori; Hokkaido University, Research Institute for Electronic Science; Hokkaido University, Graduate School of Environmental Science Shirakawa, Yuki; Hokkaido University Graduate School of Environmental Science, Sakai, Hiroki; Hokkaido University Graduate School of Environmental Science Hisaki, Ichiro; Osaka University Graduate School of Engineering Science School of Engineering Science, Noro, Shin-ichiro; Hokkaido University, Environmental Earth Science Akutagawa, Tomoyuki; Tohoku University, Institute of Multidisciplinary Research for Advanced Materials Nakano, Motohiro; Osaka Univ., Nakamura, Takayoshi; Hokkaido University, Research Institute for Electronic Science

ARTICLE

Uniaxial Negative Thermal Expansion Induced by Molecular Rotation in One-Dimensional Supramolecular Assembly with Associated Peculiar Magnetic Behavior

Received 00th January 20xx,
Accepted 00th January 20xx

DOI: 10.1039/x0xx00000x

Kiyonori Takahashi,*[a,b] Yuki Shirakawa,[b] Hiroki Sakai,[b] Ichiro Hisaki,[c] Shin-ichiro Noro,[d] Tomoyuki Akutagawa,[e] Motohiro Nakano[f] and Takayoshi Nakamura*[a,b]

In general, negative thermal expansion (NTE) is entropy-driven. We have developed the alternative approach for achieving uniaxial NTE in a molecular crystal induced by supramolecular deformation and molecular rotation, along with peculiar magnetic responses. In a crystal of (pyridazinium$^+$)$_2$(dibenzo[24]crown-8)$_3$[Ni(dmit)$_2$]$^-_2$ (**1**) (dmit = 1,3-dithiole-2-thione-4,5-dithiolate), pyridazinium was included within dibenzo[24]crown-8, and formed a one-dimensional columnar structure parallel to the *a*-axis. This column elongates along the *a*-axis, and shrinks along the *b*-axis. This provides space for the pyridazinium to rotate, which promotes further NTE above 183 K. In addition, the [Ni(dmit)$_2$]$^-$ forms dimer, where intradimer magnetic exchange interaction (*J*) increased with increasing temperature. The modified singlet-triplet thermal excitation model, where *J* increased with increasing temperature, can be fitted to the temperature-dependent magnetic susceptibility of **1**. A deviation from the model was observed above 180 K, which attributed to the structural changes within the [Ni(dmit)$_2$]$^-$ dimer, caused by the molecular rotation of the pyridazinium.

Introduction

Crystalline materials usually exhibit positive thermal expansion (PTE) with increasing temperature, owing to the increase in the anharmonic oscillation of the constituent atoms, molecules, or ions.[1,2] Materials displaying negative thermal expansion (NTE) have also been found, and can be used in conjunction with PTE materials to construct zero-thermal-expansion (ZTE) materials.[2,3] ZTE materials can be applied where thermal expansion can cause significant damage, such as in organic light-emitting diodes,[4] organic field-effect transistors,[5] fiber-optic systems, and supported catalysis.[3] However, few NTE materials have been reported thus far.[2,3,6] The $ZrW_2O_{7.91}$•$0.64NH_3$ compound shows NTE due to transverse motion perpendicular to the direction of the metal-oxide chains, known as a "guitar string" effect.[7] Similar contraction was also observed for the Sc-F chains present in ScF_3.[8] In addition to the transverse vibrational modes, NTE in molecular materials has been attributed to geometrical flexibility, e.g. through distortion of the coordination environment of metal complexes,[9–13] distortion of the coordination environment combined with ligand vibration in a direction orthogonal to the coordination direction in several metal-organic frameworks,[14–16], molecular rearrangement through the weakening of intermolecular interactions with increasing temperature,[17,18] and conformational change of the host molecule due to rearrangement of the guest molecule.[19,20]

In most cases, NTE is entropy-driven.[1,8,21,22] A typical example is seen in spin crossover (SCO) complexes.[2,23] The NTE of [Fe(bpac)(Au(CN)$_2$)$_2$]•2EtOH (bpac = 1,2-bis(4'-pyridyl)acetylene) is caused by transition of the complex from the t^6_{2g} low-spin (LS) state to the t^4_{2g} high-spin (HS) state at 230 K.[23] The Fe–N bond in the LS state is ~10% shorter than that in the higher-entropy HS state, and the NTE is caused by the smaller Au-Fe-Au angle in the HS complex than that in the LS complex. The degree of NTE can be manipulated by dilution with Ni(II). The coefficients of linear thermal expansion (CLTE) for the axis showing NTE, was decreased with increasing the fraction of Ni(II) in [Fe$_x$Ni$_{1-x}$(bpac)(Au(CN)$_2$)$_2$]•2EtOH (x = 0.25-1), where residual HS fraction below phase transition temperature was increased.[23]

Molecular motion is another important factor contributing to the increase in a system's entropy. The NTEs observed in the hydrated crystals of (H-DABCO$^+$)(Cl$^-$)•$3H_2O$ (H-DABCO$^+$ = mono

[a] Research Institute for Electronic Science (RIES), Hokkaido University, N20W10, Kita-Ward, Sapporo, Hokkaido 001-0020, Japan
[b] Graduate School of Environmental Science, Hokkaido University, N10W5, Sapporo, Hokkaido, 060-0810, Japan
[c] Graduate School of Engineering Science, Osaka University, Machikayenaya-cho 1-3, Toyonaka, Osaka, 560-8531, Japan
[d] Faculty of Environmental Earth Science, Hokkaido University, N10W5, Kita-Ward, Sapporo, Hokkaido, 060-0810, Japan
[e] Institute of Multidisciplinary Research for Advanced Materials, Tohoku University, Katahira 2-1-1, Sendai, Miyagi, 980-8577, Japan
[f] Graduate School of Science
[g] Osaka University, Machikaneyama-cho 1-3, Toyonaka, Osaka, 560-8531, Japan
† Footnotes relating to the title and/or authors should appear here.
Electronic Supplementary Information (ESI) available: Details of Crystallographiy and its temperature dependence, DSC, Input and output files of PASCal Calculation, Details of transfer integrals between [Ni(dmit) $_2$]$^-$, Expanded $\chi_m T$ *versus T* plot of Figure 5. See DOI: 10.1039/x0xx00000x

protonated 1,4-diazabicyclo[2.2.2]octane) and $(Himd^+)_2[CuCl_2]$ ($Himd^+$ = protonated imidazolium$^+$) are caused by the rotations of H_2O and $Himd^+$, respectively.[24,25] There must be sufficient space within a crystal to realize molecular rotation; however, this is generally difficult owing to the close packing of molecules in the crystal lattice.

Previously, we developed a supramolecular approach to realizing molecular rotation in the solid state. For example, in the monovalent $[Ni(dmit)_2]^-$ crystal of (*m*-fluoroanilimium$^+$)(dibenzo[18]crown-6)$[Ni(dmit)_2]^-$, *m*-fluoroanilinium$^+$ exhibits flip-flop rotation along its C–N bond. This motion is associated with the dipole moment of *m*-fluoroanilinium$^+$, derived from its C–F bond, becoming inverted collectively by outer electric field. This indicates that the flip-flop rotation is connected to the long-range ferroelectric order.

More recently, we found that dibenzo[24]crown-8 (DB[24]crown-8) is an excellent building block that provides rotational space in a crystal. Previous studies have reported that [24]crown-8 derivatives can include heteroaromatic cations within their cavities.[26–29] We previously reported the salt (H-bpy$^+$)(DB[24]crown-8)$([Ni(dmit)_2]^-$ (H-bpy$^+$ = monoprotonated 4,4'-bipyridine),[30] in which one of the pyridyl rings of H-bpy$^+$ is completely included in the DB[24]crown-8 cavity, sandwiched between its phenylene rings. The H-bpy$^+$ molecules form one-dimensional (1D) hydrogen-bonded chains, and act as pseudo-polyrotaxanes, where one of the two pyridyl rings rotates. However, including an highly-symmetric molecule within the DB[24]crown-8 cavity is expected to result in a more significant modulation effect on the crystal structure because a highly-symmetric molecule is expected to have a higher degree of freedom than the lower ones.

Herein we propose an alternate approach to developing crystalline materials that exhibit NTE and its enhancement resulting derived from a deformation of supramolecular structure and molecular rotation within the structure, respectively. Monoprotonated pyridazinium (pdazH$^+$) was chosen as the heteroaromatic cation to prepare a dynamic molecular system with DB[24]crown-8; the compound $(pdazH^+)_2(DB[24]crown\text{-}8)_3[Ni(dmit)_2]^-_2$ (**1**) was synthesized. Supramolecular deformations induced NTE along the *b*-axis to provide space for the rotation of pdazH$^+$, resulting in enhancement of the NTE. A peculiar magnetic response was observed, which was explained by the singlet-triplet (S-T) thermal excitation model, taking into account the temperature-dependent intermolecular interactions caused by NTE (Figure 1).

Results and discussion

Crystal Structure

Figure 2a shows one unit cell of the crystal structure of **1** collected at 118 K, viewed along the *a*-axis. This compound crystalizes in the monoclinic space group, $P2_1$.

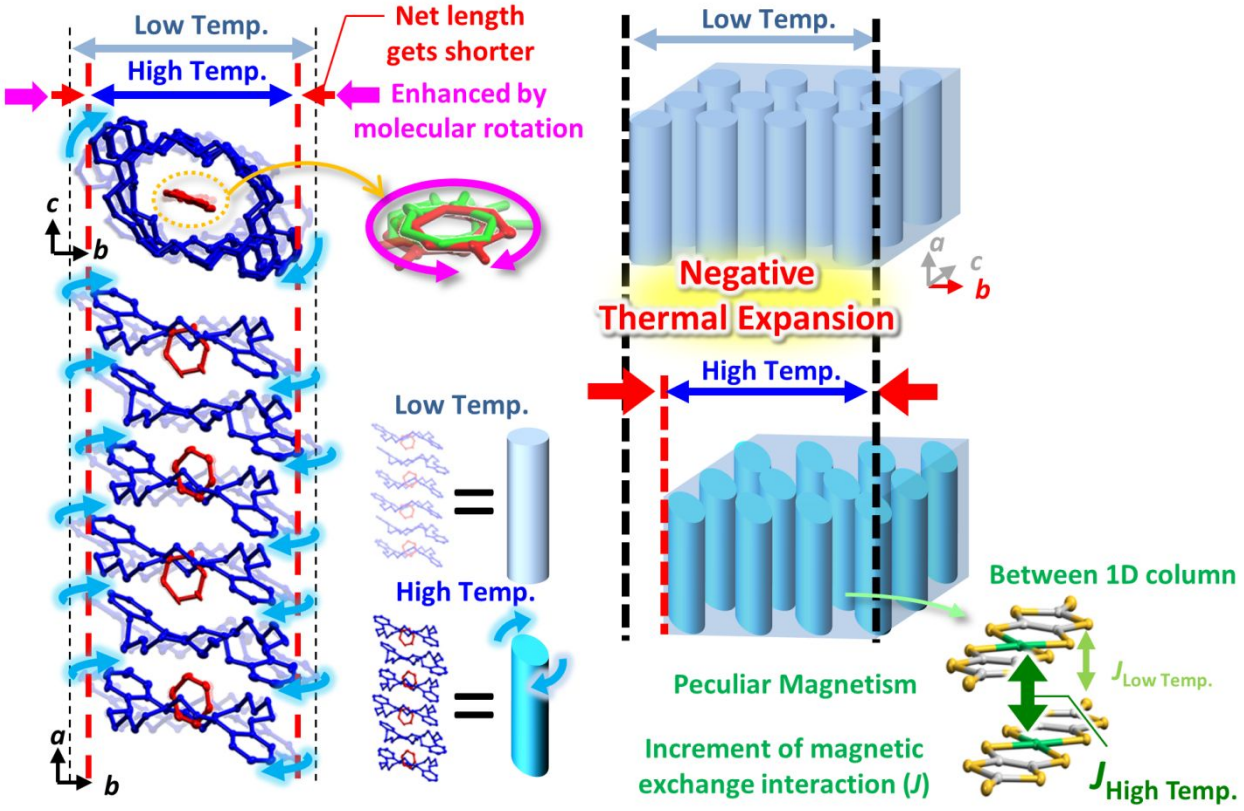

Figure 1. Schematic showing the negative thermal expansion (NTE) caused by the rotation of the supramolecular columnar structure, which in turn, is induced by the in-plane rotation by the heteroaromatic cation. The peculiar magnetism arose from the rearrangement of the $[Ni(dmit)_2]^-$ anions, causing by the NTE.

The asymmetric unit consists of two $pdaz^+$ (**PD1** and **PD2**), three DB[24]crown-8 (**DB1**, **DB2**, and **DB3**), and two $[Ni(dmit)_2]^-$ molecules, and this stoichiometry is consistent with the elemental analysis results. The crystallographically independent $pdazH^+$ and DB[24]crown-8 molecules are shown in Figure 2b. Analysis of **1** revealed that DB[24]crown-8 forms a trimer, stacked one-dimensionally to form a columnar structure along the *a*-axis. This columnar structure is stabilized through π•••π and C-H•••π interactions between the phenylene rings of adjacent molecules. The shortest C•••C distances range from 3.498(9) to 3.78(1) Å, and occur between phenylene and alkyl chains, with the shortest C•••C distance being 3.537(6) Å. Owing to its highly flexible molecular structure, **DB3** showed disorder at the oxy-ethylene moiety (labeled **DB3A** and **DB3B**, with site occupancy factors of 0.710(9) and 0.290(9) at 118 K, respectively). **PD1** and **PD2** are entirely included within the column channel formed by **DB1** and **DB2**, while **DB3A** did not encapsulate $pdazH^+$. However, weak C-H•••O contacts were observed between the ether oxygen atoms of **DB3A** and the hydrogen atoms of disordered **PD1** (**PD1A**), as shown in Figure 2c. Short contacts within **1** are summarized in Tables S2–S5 in the Supporting Information). At 118 K, the site occupancy factors for the disordered **PD1** moiety were 0.457(13) and 0.543(13), for **PD1A** and **PD1B**, respectively. Moderate hydrogen bonds[31] were observed between protonated nitrogen atoms of each of the $pdazH^+$ molecules (**PD1A**, **PD1B**, and **PD2)** and the crown ether oxygen atoms. The N1A•••O20, N1B•••O24, and N3•••O4 distances are 2.81(2), 2.93(1), and 2.81(4) Å, respectively, while the N1A-H1A•••O20, N1B-H1B•••O24, and N3-H3•••O4 angles are 172.03°, 170.89°, and 170.45°, respectively.

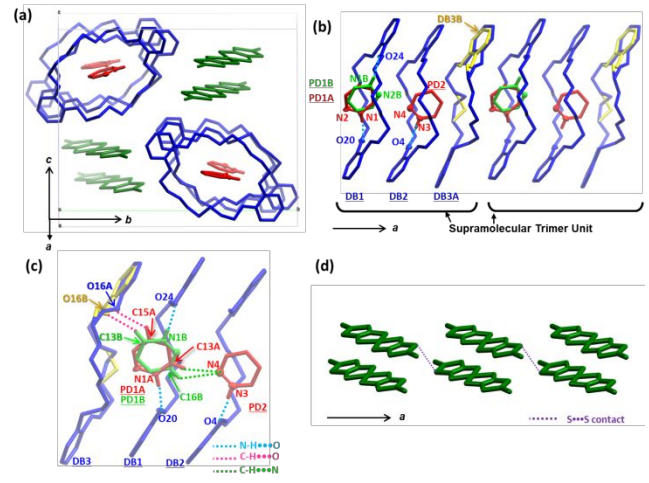

Figure 2. Crystal structure of **1** at 118 K. Molecules are depicted as capped stick models. Hydrogen atoms are omitted for clarity except those involving in N-H•••O, C-H•••O, and C-H•••N hydrogen bonding interactions. The $[Ni(dmit)_2]^-$ and DB[24]crown-8 species are colored green and blue, respectively, whereas the disordered DB[24]crown-8 sites are colored yellow. The ordered $pdazH^+$ molecule (**PD2**) and one of two sites of disordered $pdazH^+$ (**PD1A**) are colored red, and the other disordered $pdazH^+$ molecule (**PD1B**) is colored light green. (a) Packing structure of **1.** Disordered atoms omitted for clarity. (b) Supramolecular columnar structure. Crystallographically independent DB[24]crown-8 moieties are depicted as **DB1**, **DB2**, and **DB3**. (c) N-H•••O and C-H•••O interactions between $pdazH^+$ and dibenzo[24]crown-8 and C-H•••N one between $pdazH^+$ molecules, depicted as light-blue, pink- abd white-blue-dotted lines, respectively. (d) The dimeric $[Ni(dmit)_2]^-$ complexes form one-dimensional chains along the *a*-axis, connected by an S•••S interaction.

Two disordered cations, **PD1A** and **PD1B**, are oriented in such a way that they cancel out each other's dipole moments, as shown in Figure 2b. In contrast, all **PD2** molecules point in the same direction and have an overall non-zero dipole moment, which is the reason **1** adopts a non-centrosymmetric crystal structure. The $[Ni(dmit)_2]^-$ formed dimers in the spaces between the crown ether and $pdazH^+$ 1D columns, with a distance between the Ni atoms of 3.8654(7) Å. The $[Ni(dmit)_2]^-$ dimer forms S•••S contacts with adjacent dimers which propagate one-dimensionally along the *a*-axis. The shortest S–S distance between adjacent $[Ni(dmit)_2]^-$ dimers was 3.316(2) Å, which is shorter than the sum of the van der Waals radii of two sulfur atoms (3.60 Å).

Uniaxial Negative Thermal Expansion

The heat flow of crystal **1** showed a clear baseline shift to exothermic direction at 183 K in differential scanning calorimetry (DSC) measurement upon heating, indicating a second-order phase transition owing to the rotation of **PD1** (Figure S5). The temperature dependence of the unit cell volume (*V*) and axes lengths (*a*, *b*, and *c*) are displayed in Figure 3a. The *V* and length of the *a*- and *c*-axes increase with increasing temperature (with changes of 3.10, 2.32, and 1.72% between 118 and 282 K, respectively), and changes of β are -1.34% between 118 and 282 K (shown in Figures S1 and S2 in ESI), whereas the length of the *b*-axis exhibits uniaxial NTE. The CLTE of the *b*-axis in the 118–169 K temperature range is -29.65×10^{-6} K^{-1} (α_{b1}). However, at the higher temperature range of 186–282 K, the CLTE value approximately triples to -81.25×10^{-6} K^{-1} (α_{b2}) owing to the conformational changes of **DB3** and the molecular rotation of **PD1** in crystal **1**. Figure 3b summarizes the molecular structures of **PD1** and **DB3** at 118 and 282 K.

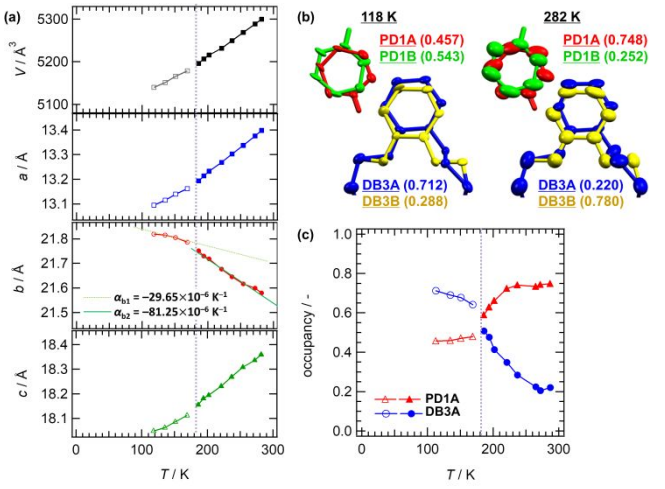

Figure 3. Temperature dependence of structural parameters of crystal 1. Opened and closed symbols correspond to data measured below and above the phase transition temperature (183 K, which is represented as purple-dotted line),

respectively. (a) unit-cell volume and parameters. (b) Molecular structures of PD1 and DB3 from crystal structures were collected at 118 and 282 K, with atoms shown as thermal ellipsoids at 50% probability. (c) Site occupancy factors of PD1A and DB3A at various temperatures of structure collection.

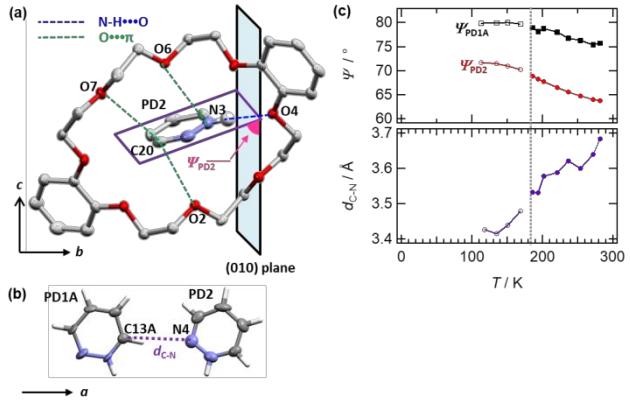

Figure 4. Schematic of selected parameters in supramolecular cation structure. Oxygen carbon, and nitrogen atoms are depicted as red, gray and blue, respectively. Several hydrogen atoms are omitted for clarity. The atoms are displayed using the thermal ellipsoid model. (a) Schematic of Ψ_{PD2}, the inter-planer angle between the molecular plane of **PD2** and the (010) plane. Displayed are the N-H•••O hydrogen bond, and multiple O•••π interactions that occur between **PD2** and **DB2**. (b) Schematic of the interaction (purple) between C13A in **PD1A** and N4 in **PD2** ($d_{C\text{-}N}$). (c) Temperature dependences of Ψ_{PD1A} (black), Ψ_{PD2} (red), and $d_{C\text{-}N}$ (purple). The dashed line corresponds to the phase transition temperature of 183 K.

The increase in the thermal fluctuation of atoms is indicated by the larger atomic thermal ellipsoids in both **PD1** and **DB3** at 282 K, and suggests an increase in molecular motion of **PD1** and **DB3** at higher temperatures. The temperature dependences of the atomic site occupancy factors of **PD1A** and **DB3A** are shown in Figure 3c. The site occupancy factor of **PD1A** showed a sharp increase when the temperature was raised to 186 K, increases steadily on increasing the temperature further, and reaches approximately 0.75 at temperatures above 221 K. In contrast, the site occupancy factor of **DB3A** decreases with increasing temperature. From 118 K, the site occupancy factor of 0.712(1) decreases gradually until 186 K, after which a steeper decrease to 0.220(19) at 282 K was observed. Since the rotation of **PD1** causes the site occupancy factor of **DB3A** to change, it indicates that the motion of **PD1** correlates to the displacement of **DB3** through weak C-H•••O interactions.

To elucidate the relationship between the change in the macroscopic crystal structure and the molecular motions of **PD** and **DB**, we investigated the temperature dependence of the interplanar angles between the (010) plane and molecular planes of **PD1A** and **PD2** (Ψ_{PD1A} and Ψ_{PD2}, respectively), which are shown in Figure 4a (corresponding one for **PD1B** (Ψ_{PD1B}) are shown in Figure S6 in ESI). The results are presented in Figure 4b, and show that these interplanar angles are directly related to the length of the *b*-axis. At 118 K, Ψ_{PD1A} and Ψ_{PD2} were 79.87° and 71.69°, respectively. The angles decrease with increasing temperature, and at 282 K reach 75.71 and 63.72°, respectively, meaning that the molecular planes of both pdazH$^+$ ions tilt towards the (010) plane with increasing temperature. Because the multiple O•••π interactions[32] and the N-H•••O hydrogen bonds between **DB2** and **PD2** remain unchanged between 118 and 282 K (bonds shown in Figure 4a, details given in Tables S4–S5), the DB[24]crown-8 molecule must have followed the motion of pdazH$^+$ and also tilted toward the (010) plane as the temperature increased. This motion corresponds to the rotation of DB[24]crown-8 about its long axis to align with the *c*-axis. Similarly, **PD1** and **DB1** also exhibit the same tilting behavior as the temperature varies. Through this tilting, the width of the supramolecular column decreases in the direction of the *b*-axis, giving **1** a uniaxial NTE. In contrast, the length of the *a*-axis increases with increasing temperature, and corresponds to the elongation of the 1D supramolecular column. The C13A•••N4 distance ($d_{C\text{-}N}$), corresponding to the C-H•••N hydrogen bond between **PD1A** and **PD2** (shown in Figure 4b), increased from 3.476 Å at 169 K to 3.532 Å at 186 K (Figure 4c). **DB3A** interacts with **PD1** through a weak C-H•••O hydrogen bond. However, increasing the temperature caused the site occupancy factor of **DB3A** to decrease from 0.712(1) at 118 K to 0.220(19) at 282 K, with a corresponding increase in the site occupancy factor of **DB3B**. The conformation of **DB3B** is such that there are no C-H•••O interactions between **DB3B** and **PD1A**, which allows for the rotation of **PD1** within the channels. When **PD1** rotates, the system's entropy increases, and the crystal becomes more stable. This energy gain is the driving force for the entire deformation process and subsequent NTE along the *b*-axis. These results add to the body of work showing that supramolecular deformation triggered by molecular rotation is a novel mechanism for realizing the uniaxial NTE of a crystal.

Magnetic Property

Figure 5 shows the temperature dependence of the molar magnetic susceptibility (χ_m) of a polycrystalline sample of **1**. From structural analysis, the dominant magnetic exchange interaction (*J*) originates from the $[Ni(dmit)_2]^-$•••$[Ni(dmit)_2]^-$ intradimer interaction (see Figure S7 in ESI). According to previous reports, the measured $\chi_m T$ values were fitted using the S-T thermal excitation model[33] for magnetically isolated $[Ni(dmit)_2]^-$ dimer.[34,35] Below 30 K, the experimental data is well-fitted to the S-T model (black line, Figure 5) and gives

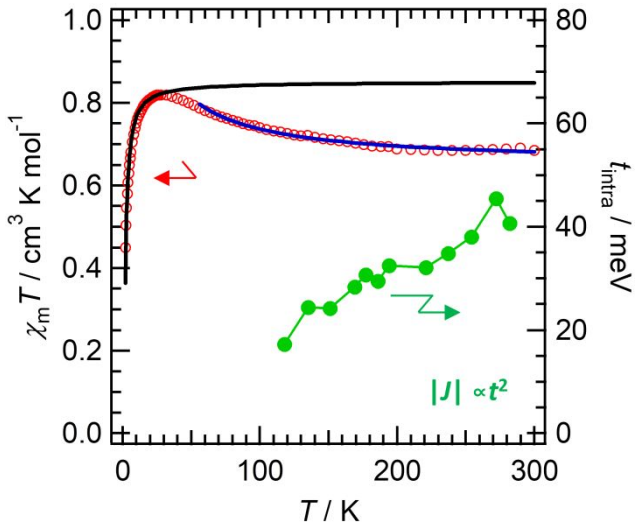

Figure 5. Temperature-dependent molar magnetic susceptibility ($\chi_m T$, left scale) of crystal **1**. The black and blue lines indicate the best fits at different temperature ranges using the S-T thermal excitation model; the equations have an associated J/k_B = –1.85 and (–0.396 T + 15.5) K, respectively. Both models have an associated Landé g-factor of 2.13. Intradimer transfer integral (t_{intra}, right scale). The absolute value of magnetic exchange interaction (J) in the S-T model is proportional to t squared, i.e., ($|J| \propto t^2$).

g = 2.13 and J/k_B = −1.85 K, where g and k_B are the Landé g-factor and Boltzmann constant, respectively. However, from 30 to 300 K, the $\chi_m T$ values were smaller than those predicted by the model. Therefore, in this temperature range, we applied a modified S-T model with a temperature-dependent J,[36,37] using $J/k_B = c_0 T + c_1$, where c_0 and c_1 are constants. From 60 to 300 K, the $\chi_m T$ values can be fitted with g = 2.13 and J/k_B = −0.396 T + 15.5; however, between 180 and 280 K, the experimental $\chi_m T$ values were slightly smaller than those predicted by the model (Figure S8 in Supporting Information). We evaluated the magnetic behavior of **1** as a function of the temperature-dependent transfer integral (t), as the absolute value of J is proportional to t squared, i.e., ($|J| \propto t^2$).[38–40] The temperature dependence calculations of the intradimer t (t_{intra}) between $[Ni(dmit)_2]^-$ anions were made using the $[Ni(dmit)_2]^-$ coordinates obtained from the single-crystal X-ray structures collected at various temperatures (Figure 5, green, left axis). At 118 K, t_{intra} was calculated to be 17.2 meV, and increased as the temperature was raised, finally reaching 40.7 meV at 282 K. Using the calculated t_{intra} values and $|J| \propto t^2$, the value of J at 282 K is approximately 5.6 times larger than that at 118 K. The ratio of J/k_B at 118 and 282 K is 3.1 when calculated using J/k_B = –0.396 T +15.5. The increase in J with increasing temperature

is roughly consistent with the increasing trend of t^2. Therefore, we can conclude that the peculiar temperature dependence of the magnetic susceptibility is due to the structural changes within the $[Ni(dmit)_2]^-$ dimer, which results in a temperature-dependent t.

Relationship between structural change, NTE, and magnetism

To further clarify the relationship between the temperature-induced structural change of the $[Ni(dmit)_2]^-$ dimer and the accompanying uniaxial NTE, we focused on the temperature dependence of the angles between S3•••S4•••S14 and S8•••S9•••S19, located within the $[Ni(dmit)_2]^-$ dimer as shown in Figure 6a (denoted as $\Phi_{S3\text{-}S4\text{-}S14}$ and $\Phi_{S8\text{-}S9\text{-}S19}$, respectively). These angles have been plotted as a function of temperature in Figure 6b. At 118 K, the $[Ni(dmit)_2]^-$ ions within the dimer overlap, with concomitant angles, $\Phi_{S3\text{-}S4\text{-}S14}$ and $\Phi_{S8\text{-}S9\text{-}S19}$, equal to 110.97° and 108.40°, respectively. As the temperature increases, the cationic supramolecular column expands, causing the phenylene ring of DB[24]crown-8 to push the two $[Ni(dmit)_2]^-$ anions to better overlap. This is evidenced by $\Phi_{S3\text{-}S4\text{-}S14}$ and $\Phi_{S8\text{-}S9\text{-}S19}$ decreasing monotonically, reaching 106.19° and 106.10° at 282 K, respectively. The angles, $\Phi_{S3\text{-}S4\text{-}S14}$ and $\Phi_{S8\text{-}S9\text{-}S19}$, decrease more steeply after the temperature is raised to 186 K, but the rate of the concomitant monotonic increase of t is unaffected. However, the increase in t_{intra} does correspond to the increase in the magnitude of J at higher temperatures (Figure 5). Therefore, the molecular rotation of **PD1** at temperatures above 183 K accelerates the deformation of the supramolecular assembly, resulting in the decrease in the $\chi_m T$ value from the theoretical value.

In summary, the deformation of the supramolecular structure by rotation of $pdazH^+$ cation results in the enhancement of NTE of the b-axis, and the improved overlap of the $[Ni(dmt)_2]^-$ dimer, the latter which causes the small deviation of $\chi_m T$ from the theoretical model in the temperature range from 180 to 280 K.

Experimental Section

Preparation

Precursors of $(TBA)^+[Ni(dmit)_2]^-$, (where TBA = tetra-*n*-butylammonium) was obtained according to the literature methods.[41] Crystal **1**: $(pdaz^+)(BF_4^-)$ (50 mg, 2.98×10^{-1} mmol) and DB[24]crown-8 (200 mg, 4.45×10^{-1} mmol) were dissolved in 30 mL acetone and mixed in 20 mL acetone solution of $(TBA)^+[Ni(dmit)_2]^-$ (20 mg, 2.8×10^{-2} mmol) with stirring. Acetone solution was evaporated in ambient condition and black crystals were obtained after one week. Elemental analysis for crystal **1**, calcd for $C_{92}H_{106}N_4Ni_2O_{24}S_{20}$: C: 45.84%

ARTICLE

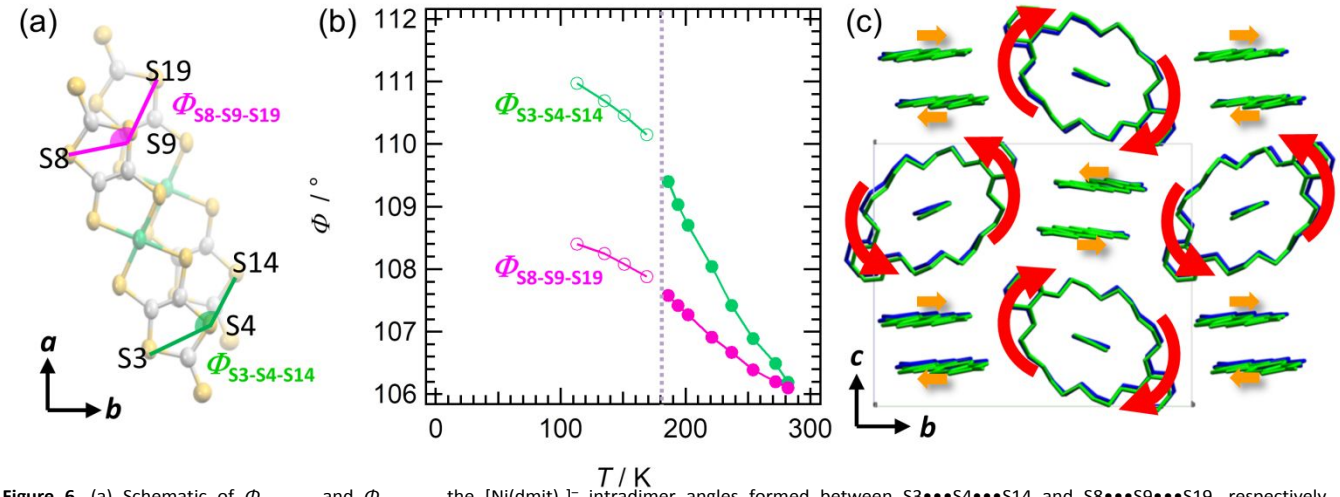

Figure 6. (a) Schematic of $\Phi_{S3\text{-}S4\text{-}S14}$ and $\Phi_{S8\text{-}S9\text{-}S19}$, the $[Ni(dmit)_2]^-$ intradimer angles formed between S3•••S4•••S14 and S8•••S9•••S19, respectively. (b) Temperature dependence of $\Phi_{S3\text{-}S4\text{-}S14}$ and $\Phi_{S8\text{-}S9\text{-}S19}$. The dashed line corresponds to phase transition temperature at 183 K. (c) Superimposed crystal packing of **1** at 118 K (blue) and 282 K (green), viewed down the *a*-axis. The red and orange arrows indicate the respective directions in which the DB[24]crown-8 and $[Ni(dmit)_2]^-$ species move as the temperature is increased.

H: 4.43% N: 2.32% Found: C: 45.87% H: 4.38%, N: 2.25%. Elemental analysis for crystal **1**, calcd for $C_{92}H_{106}N_4Ni_2O_{24}S_{20}$: C: 45.84% H: 4.43% N: 2.32% Found: C: 45.87% H: 4.38%, N: 2.25%.

Crystal Structure Determination

Temperature-dependent structural analysis of the single crystal **1** were performed in a Rigaku XtaLAB-Synergy diffractometer with a HyPix-6000 area detector and a multilayer mirror-monochromated Mo Kα radiation (λ= 0.71073 Å). A single crystal was mounted on MicroMountsTM tip (MiTeGen) with Paratone 8277 (Hampton Research). Temperature dependence was measured on the same crystal. For the reflection data, multi-scan absorption corrections were applied to the crystal**s**. Data collection was performed and processed with CrysAlisPRO (Oxford Diffraction, Agilent Technologies UK Ltd). The initial structure was solved by SHELXT,[42] and structural refinement was performed by using OLEX2 software.[43] Anisotropic refinement was applied to all atoms, except the hydrogen atoms. The structure was refined as 2-component inversion twin for crystal **1**. These data are provided free of charge in The Cambridge Crystallographic Data Centre (CCDC No. 2163119, 2163120, 2163121, 2163122, 2163123, 2163124, 2163125, 2163126, 2163127, 2163128, 2163129, 2163130, and 2163131 for crystals **1** at 118, 135, 151, 169, 177, 186, 194, 202, 221, 237, 254, 272 and 282 K, respectively.

Thermal Analysis.

Differential scanning calorimetry (DSC) measurement was carried out with a Q2000 differential scanning calorimeter (TA Instruments) in the temperature range from 150 to 290 K at a scanning rate of 5 K·min^{-1} under a flow of N_2 gas flow (50 mL·min^{-1}).

Magnetic Measurement.

The temperature–dependent magnetic susceptibility for a polycrystalline sample of **1** was measured with a Quantum Design MPMS-3 SQUID magnetometer. Prior to sample measurement, magnetic susceptibility of the sample holder (plastic wrap) was measured under identical conditions, then the susceptibility of the holder subtracted from the gram susceptibility as the diamagnetic contribution. Diamagnetic contribution of the diamagnetic component in the sample was subtracted based on the Pascal's constant, -1.02916×10^{-3} cm^3 mol^{-1}.[44] A magnetic field of 1 T was applied for all temperature-dependent measurements. Molecular weight of 2410.42 g mol^{-1} (molar susceptibility per two $[Ni(dmit)_2]^-$ molecules) was used for the calculation of molar magnetic susceptibility of crystal **1**.

Theoretical Calculations.

The extended Hückel molecular orbital method within the tight-binding approximation was applied to calculate the

transfer integrals (*t*) between $[Ni(dmit)_2]^-$ anions in the crystal **1**. The lowest unoccupied molecular orbital of the $[Ni(dmit)_2]^-$ molecule was used as the basis function.[45] According to the literature, semiempirical parameters for Slater-type atomic orbitals were obtained.[45] The *t* values between each pair of molecules were assumed to be proportional to the overlap integral (S) according to the equation $t = -10S$ eV. Coefficient of linear thermal expansion for the *b* axis was calculated by *PASCal* web program based on the unit cell parameters at each temperatures.[46]

Conclusions

This paper reports a novel approach for realizing uniaxial NTE by supramolecular motion in a magnetic $[Ni(dmit)_2]^-$ salt, and accounts for the associated peculiar magnetic response. The cause of NTE is in contrast to previously reported materials, which undergo NTE mainly due to transverse vibration, conformational change, geometric flexibility, and spin crossover, which are all related to covalent interactions.[2]

We report that at temperatures above 183 K, the organic cation within **1** rotates, causing the supramolecular column structure to deform. This deformation enhances NTE of the crystal's *b*-axis, and the improved overlap of the $[Ni(dmt)_2]^-$ ions within the dimer, enhancing the dimer's magnetic interaction. The latter causes the small deviation of $\chi_m T$ from the theoretical model in the temperature range from 180 to 280 K.

The use of supramolecular cations, formed from macrocyclic crown ether rings and organic cations, are expected to be relatively easy to prepare. They are additionally expected to exhibit molecular motion, which is usually difficult in the crystalline phase. These supramolecular cations can be combined with anions having various functionalities, making them more versatile than conventional materials exhibiting molecular motion-type NTEs. Our research group is making progress in constructing NTE materials based on supramolecular approaches, and developing materials with peculiar physical properties.

Author Contributions

Y.S. and H.S. performed the synthesis of the compound **1**. Y.S. acquired and S.N. analysed the thermal data. K.T. performed crystallography, acquired the magnetic data, and calculated transfer integral. M.N. and K.T. analysed and interpreted the magnetic data. I.H. interpreted the crystallographic data. T.A. interpreted the calculation result of transfer integral. T.N. and K.T. conceived and compiled the idea for the research and analysed and interpreted all data. The first manuscript was written by K.T. and T.N. and edited by all authors.

Conflicts of interest

There are no conflicts to declare.

Acknowledgements

We thank Ms. Ai Tokumitsu of Global Facility Center, Hokkaido University for elemental analysis, Dr. Shuhei Fukuoka and Dr. Satoaki Matsunaga of Faculty of Science, Hokkaido University for magnetic measurement. This study was supported financially by JSPS KAKENHI (grant no. JP18H01949, JP22H00311 and JP21K14691), JSPS Joint Research Projects under the Bilateral Programs (grant no. 120197402), "Dynamic Alliance for Open Innovation Bridging Human, Environment and Materials", and Research Program of "Network Joint Research Center for Materials and Devices: Dynamic Alliance for Open Innovation Bridging Human, Environment and Materials", from the Ministry of Education, Culture, Sports, Science and Technology of Japan (MEXT), and JST CREST (grant no. JPMJCR18I4), Japan. This research was also supported finantially by Murata Science Foundation, Iketani Science and Technology Foundation, and Harmonic Ito Foundation.

Notes and references

1 P. J. Attfield, *Front. Chem.*, 2018, **6**, 371.
2 Z. Liu, Q. Gao, J. Chen, J. Deng, K. Lin and X. Xing, *Chem. Commun.*, 2018, **54**, 5164–5176.
3 J. Chen, L. Hu, J. Deng and X. Xing, *Chem. Soc. Rev.*, 2015, **44**, 3522–3567.
4 X. Ge, Y. Mao, X. Liu, Y. Cheng, B. Yuan, M. Chao and E. Liang, *Sci. Rep.*, 2016, **6**, 24832.
5 M. Yokota, Y. Hisakado, H. Yang, T. Kajiyama, N. Mater, H. Kikuchi, T. Nagamura, A. Mater, M. J. Sansone, G. Khanarian, T. M. Leslie, M. Stiller, J. Altman, P. Elizondo, D. Gottke, D. D. Brace, H. Cang, B. Bagchi, M. D. Fayer, J. Chem, B. Thokchom Birendra Singh, F. Meghdadi, S. Günes, N. Marjanovic, G. Horowitz, P. Lang, S. Bauer and N. Serdar Sariciftci, *Adv. Mater.*, 2005, **17**, 2315–2320.
6 S. Zhu, P. Wu, H. Yelemulati, J. Hu, G. Li, L. Li and Y. Tai, *Matter*, 2021, **4**, 1832–1862.
7 W. Cao, Q. Huang, Y. Rong, Y. Wang, J. Deng, J. Chen and X. Xing, *Inorg. Chem. Front.*, 2016, **3**, 856–860.
8 D. Wendt, E. Bozin, J. Neuefeind, K. Page, W. Ku, L. Wang, B. Fultz, A. V. Tkachenko and I. A. Zaliznyak, *Sci. Adv.*, 2019, **5**, eaay2748.
9 R. Ohtani, A. Grosjean, R. Ishikawa, R. Yamamoto, M. Nakamura, J. K. Clegg and S. Hayami, *Inorg. Chem.*, 2017, **56**, 6225–6233.
10 R. Ohtani, R. Yamamoto, T. Aoyama, A. Grosjean, M. Nakamura, J. K. Clegg and S. Hayami, *Inorg. Chem.*, 2018, **57**, 11588–11596.
11 R. Ohtani, R. Yamamoto, H. Ohtsu, M. Kawano, J. Pirillo, Y. Hijikata, M. Sadakiyo, L. F. Lindoy and S. Hayami, *Dalton Trans.*, 2019, **48**, 7198–7202.
12 R. Ohtani, J. Yanagisawa, H. Matsunari, M. Ohba, L. F. Lindoy and S. Hayami, *Inorg. Chem.*, 2019, **58**, 12739–12747.
13 R. Ohtani, J. Yanagisawa, B. Le Ouay and M. Ohba, *ChemNanoMat*, 2021, **7**, 534–538.
14 Y. Wu, A. Kobayashi, G. J. Halder, V. K. Peterson, K. W. Chapman, N. Lock, P. D. Southon, C. J. Kepert, Y. Wu, A. Kobayashi, G. J. Halder, V. K. Peterson, N. Lock, P. D. Southon, C.

J. Kepert and K. W. Chapman, *Angew. Chemie Int. Ed.*, 2008, **47**, 8929–8932.

15 N. Lock, Y. Wu, M. Christensen, L. J. Cameron, V. K. Peterson, A. J. Bridgeman, C. J. Kepert and B. B. Iversen, *J. Phys. Chem. C*, 2010, **114**, 16181–16186.

16 A. W. Thornton, R. Babarao, A. Jain, F. Trousselet and F. X. Coudert, *Dalton Trans.*, 2016, **45**, 4352–4359.

17 R. H. Jones, K. S. Knight, W. G. Marshall, J. Clews, R. J. Darton, D. Pyatt, S. J. Coles and P. N. Horton, *CrystEngComm*, 2014, **16**, 237–243.

18 D. Das, T. Jacobs and L. J. Barbour, *Nat. Mater.*, 2010, **9**, 36–39.

19 H.-L. Zhou, Y.-B. Zhang, J.-P. Zhang and X.-M. Chen, *Nat. Commun.*, 2015, **6**, 6917.

20 H.-L. Zhou, R.-B. Lin, C.-T. He, Y.-B. Zhang, N. Feng, Q. Wang, F. Deng, J.-P. Zhang and X.-M. Chen, *Nat. Commun.*, 2013, **4**, 2534.

21 Z. K. Liu, Y. Wang and S. L. Shang, *Sci. Rep.*, 2014, **4**, 7043.

22 B. Mu and K. S. Walton, *J. Phys. Chem. C*, 2011, **115**, 22748–22754.

23 B. R. Mullaney, L. Goux-Capes, D. J. Price, G. Chastanet, J.-F. Létard and C. J. Kepert, *Nat. Commun.*, 2017, **8**, 1053.

24 M. Szafrański, *J. Mater. Chem. C*, 2013, **1**, 7904–7913.

25 Z.-S. Yao, H. Guan, Y. Shiota, C.-T. He, X.-L. Wang, S.-Q. Wu, X. Zheng, S.-Q. Su, K. Yoshizawa, X. Kong, O. Sato and J. Tao, *Nat. Commun.*, 2019, **10**, 4805.

26 S. J. Loeb and D. A. Tramontozzi, *Org. Biomol. Chem.*, 2005, **3**, 1393–1401.

27 S. J. Loeb and J. A. Wisner, *Chem. Commun.*, 1998, 2757–2758.

28 N. Georges, S. J. Loeb, J. Tiburcio and J. A. Wisner, *Org. Biomol. Chem.*, 2004, **2**, 2751–2756.

29 S. J. Loeb and J. A. Wisner, *Chem. Commun.*, 2000, 845–846.

30 Y. Shirakawa, K. Takahashi, H. Sato, N. Hoshino, H. Anetai, S. Noro, T. Akutagawa and T. Nakamura, *Chem. – A Eur. J.*, 2019, **25**, 6920–6927.

31 G. A. Jeffrey, *An Introduction to Hydrogen Bonding*, Oxford University Press, New York, 1997.

32 J. Hwang, P. Li, M. D. Smith, C. E. Warden, D. A. Sirianni, E. C. Vik, J. M. Maier, C. J. Yehl, C. D. Sherrill and K. D. Shimizu, *J. Am. Chem. Soc.*, 2018, **140**, 13301–13307.

33 Brebis Bleaney and K.D. Bowers, *Proc. R. Soc. London. Ser. A. Math. Phys. Sci.*, 1952, **214**, 451–465.

34 T. Akutagawa, K. Shitagami, S. Nishihara, S. Takeda, T. Hasegawa, T. Nakamura, Y. Hosokoshi, K. Inoue, S. Ikeuchi, Y. Miyazaki and K. Saito, *J. Am. Chem. Soc.*, 2005, **127**, 4397–4402.

35 S. Nishihara, T. Akutagawa, T. Hasegawa and T. Nakamura, *Chem. Commun.*, 2002, **2**, 408–409.

36 S. L. Veber, M. V. Fedin, K. Y. Maryunina, A. Potapov, D. Goldfarb, E. Reijerse, W. Lubitz, R. Z. Sagdeev, V. I. Ovcharenko and E. G. Bagryanskaya, *Inorg. Chem.*, 2011, **50**, 10204–10212.

37 C. P. Constantinides, E. Carter, D. M. Murphy, M. Manoli, G. M. Leitus, M. Bendikov, J. M. Rawson and P. A. Koutentis, *Chem. Commun.*, 2013, **49**, 8662.

38 J. C. Scott, in *Semiconductors and Semimetals*, Elsevier, 1988, vol. 27, pp. 385–436.

39 T. Akutagawa, T. Nakamura, T. Inabe and A. E. Underhill, *Thin Solid Films*, 1998, **331**, 264–271.

40 T. Akutagawa and T. Nakamura, *Coord. Chem. Rev.*, 2002, **226**, 3–9.

41 G. Steimecke, H.-J. Sieler, R. Kirmse and E. Hoyer, *Phosphorous Sulfur Relat. Elem.*, 1979, **7**, 49–55.

42 G. M. Sheldrick, *Acta Crystallogr. Sect. A Found. Adv.*, 2015, **71**, 3–8.

43 O. V Dolomanov, L. J. Bourhis, R. J. Gildea, J. A. K. Howard and H. Puschmann, *J. Appl. Crystallogr.*, 2009, **42**, 339–341.

44 G. A. Bain and J. F. Berry, *J. Chem. Educ.*, 2008, **85**, 532–536.

45 T. Mori, A. Kobayashi, Y. Sasaki, H. Kobayashi, G. Saito and H. Inokuchi, *Bull. Chem. Soc. Jpn.*, 1984, **57**, 627–633.

46 M. J. Cliffe and A. L. Goodwin, *J. Appl. Crystallogr.*, 2012, **45**, 1321–1329.